

SG-GS: Photo-realistic Animatable Human Avatars with Semantically-Guided Gaussian Splatting

Haoyu Zhao^{*1,2}, Chen Yang^{*1}, Hao Wang^{*3}, Xingyue Zhao⁴, Wei Shen^{†1}

¹MoE Key Lab of Artificial Intelligence, AI Institute, Shanghai Jiao Tong University

²School of Computer Science, Wuhan University,

³Wuhan National Laboratory for Optoelectronics, Huazhong University of Science and Technology,

⁴School of Software Engineering, Xi'an Jiao Tong University,,

haoyu.zhao@whu.edu.cn, ycyangchen@sjtu.edu.cn, wanghao020110@hust.edu.cn, zhaoxingyue@stu.xjtu.edu.cn, wei.shen@sjtu.edu.cn

Abstract

Reconstructing photo-realistic animatable human avatars from monocular videos remains challenging in computer vision and graphics. Recently, methods using 3D Gaussians to represent the human body have emerged, offering faster optimization and real-time rendering. However, due to ignoring the crucial role of human body semantic information which represents the intrinsic structure and connections within the human body, they fail to achieve fine-detail reconstruction of dynamic human avatars. To address this issue, we propose **SG-GS**, which uses semantics-embedded 3D Gaussians, skeleton-driven rigid deformation, and non-rigid cloth dynamics deformation to create photo-realistic animatable human avatars from monocular videos. We then design a Semantic Human-Body Annotator (SHA) which utilizes SMPL’s semantic prior for efficient body part semantic labeling. The generated labels are used to guide the optimization of Gaussian semantic attributes. To address the limited receptive field of point-level MLPs for local features, we also propose a 3D network that integrates geometric and semantic associations for human avatar deformation. We further implement three key strategies to enhance the semantic accuracy of 3D Gaussians and rendering quality: semantic projection with 2D regularization, semantic-guided density regularization and semantic-aware regularization with neighborhood consistency. Extensive experiments demonstrate that **SG-GS** achieves state-of-the-art geometry and appearance reconstruction performance. The code will be made available.

Introduction

Creating photo-realistic, animatable human avatars from monocular videos has substantial implications for gaming (Zackariasson and Wilson 2012), extended reality storytelling (Healey et al. 2021), and tele-presentation (Ho et al. 2023). In this work, we are dedicated to create high-quality photo-realistic, animatable human avatars from monocular videos with semantics embedded 3D Gaussians.

Recent advances in implicit neural fields (Mildenhall et al. 2021; Oechsle, Peng, and Geiger 2021; Niemeyer et al.

2020; Wang et al. 2022a; Sitzmann et al. 2021) enable high-quality reconstruction of geometry (Xu, Alldieck, and Sminchisescu 2021; Wang et al. 2022b; Guo et al. 2023) and appearance (Jiang et al. 2022; Li et al. 2022; Raj et al. 2021; Yu et al. 2023; Weng et al. 2022) of clothed human bodies from sparse multi-view or monocular videos. However, they often employ large MLPs, which makes training and rendering computationally demanding and inefficient.

Point-based rendering (Rückert, Franke, and Stamminger 2022; Su, Bagautdinov, and Rhodin 2023; Zheng et al. 2023) has emerged as an efficient alternative to NeRFs, offering significantly faster rendering. The recently proposed 3D Gaussian Splatting (3DGS) (Kerbl et al. 2023) achieves state-of-the-art novel view synthesis performance on static scenes with significantly reduced inference time and faster training. 3DGS has inspired several recent works in animatable human avatar creation (Lei et al. 2024; Moreau et al. 2024; Shao et al. 2024; Hu et al. 2024b; Kocabas et al. 2024; Wang et al. 2024; Qian et al. 2024; Hu et al. 2024a). However, these methods often overlook crucial semantic information that represents the connections within the human body, leading to issues in maintaining anatomical coherence during motion and preserving fine details such as muscle definition and skin folds in various poses.

To this end, we propose **SG-GS**, a Semantically-Guided 3D human model using Gaussian Splatting representation. Our **SG-GS** first integrates a skeleton-driven rigid deformation, and a non-rigid cloth dynamics deformation to coordinate the movements of individual Gaussians during animation. We then introduce a Semantic Human-Body Annotator (SHA), which leverages SMPL’s (Loper et al. 2015) human semantic prior for efficient body part semantic labeling. These part labels are used to guide the optimization of 3D Gaussian’s semantic attribute. Point-level MLPs have a limited receptive field for capturing local geometric and semantic features. To address this, we propose a 3D geometry- and semantic-aware network to learn body geometric and semantic associations and integrate them into the avatar deformation. We further implement three key strategies to enhance semantic accuracy of 3D Gaussians and rendering quality: semantic projection with 2D regularization, semantic-guided density regularization and semantic-aware regularization with neighborhood consistency. Our

Copyright © 2025, Association for the Advancement of Artificial Intelligence (www.aaai.org). All rights reserved.

^{*}Equal contributions.

[†]Corresponding Author.

Haoyu Zhao completed this work during an internship at Shanghai Jiao Tong University.

experimental results demonstrate that **SG-GS** achieves superior performance compared to current state-of-the-art approaches (Qian et al. 2024; Hu et al. 2024b,a) in animatable avatar creation from monocular inputs.

In summary, our work makes the following contributions:

- We propose **SG-GS**, which is the first to integrate semantic priors from the human body into creating animatable human avatars from monocular videos.
- We propose a 3D geometry- and semantic-aware network to capture detailed local geometric and semantic information about the human body.
- We introduce semantic projection with 2D regularization, semantic-aware regularization with neighborhood consistency, and semantic-guided density regularization to improve semantic accuracy and rendering quality.

Related Work

Neural Rendering for Human Avatars

Since the introduction of Neural Radiance Fields (NeRF) (Mildenhall et al. 2021), there has been a surge of research on neural rendering for human avatars (Li et al. 2022; Liu et al. 2021; Li et al. 2023; Peng et al. 2021b; Wang et al. 2022b). Though, NeRF is designed for static objects, HumanNeRF (Weng et al. 2022) extend the NeRF to enable capturing a dynamic moving human using just a single monocular video. Neural Body (Peng et al. 2021b) associates a latent code to each SMPL (Loper et al. 2015) vertex to encode the appearance, which is transformed into observation space based on the human pose. Furthermore, Neural Actor (Liu et al. 2021) learns a deformable radiance field with SMPL (Loper et al. 2015) as guidance and utilizes a texture map to improve its final rendering quality. Posevocab (Li et al. 2023) designs joint-structured pose embeddings to encode dynamic appearances under different key poses, enabling more effective learning of joint-related appearances. However, a major limitation of NeRF-based methods is that NeRFs are slow to train and render.

Some works focus on achieving fast inference and training times for NeRF models of human avatars, including approaches that use explicit representations such as learning a function at grid points (Chen et al. 2022; Reiser et al. 2021), using hash encoding (Müller et al. 2022), or altogether discarding the learnable component (Fridovich-Keil et al. 2022). iNGP (Müller et al. 2022) uses the underlying representation for articulated NeRFs, and enable interactive rendering speeds (15 FPS). (Chen et al. 2023) generates a pose-dependent UV volume, but its UV volume generation is not fast (20 FPS). In contrast to all these works, **SG-GS** achieves state-of-the-art rendering quality and speed (25 FPS) with less training time from monocular video inputs.

Dynamic 3D Gaussians for Human Avatars

Point-based rendering (Rückert, Franke, and Stamminger 2022; Su, Bagautdinov, and Rhodin 2023; Zheng et al. 2023) has proven to be an efficient alternative to NeRFs for fast inference and training. Extending point clouds to 3D Gaussians, 3D Gaussian Splatting (3DGS) (Kerbl et al. 2023)

models the rendering process by splatting a set of 3D Gaussians onto the image plane via alpha blending. This approach achieves state-of-the-art rendering quality with real-time inference speed for novel views and fast training.

Given the impressive performance of 3DGS in both quality and speed, numerous works have further explored the 3D Gaussian representation for dynamic scene reconstruction. D-3DGS (Luiten et al. 2024) is proposed as the first attempt to adapt 3DGS into a dynamic setup. Other works (Wu et al. 2024; Yang et al. 2024b; Zhao et al. 2024) model 3D Gaussian motions with a compact network or 4D primitives, resulting in highly efficient training and real-time rendering.

The application of 3DGS in dynamic 3D human avatar reconstruction is just beginning to unfold (Jiang et al. 2024; Lei et al. 2024; Qian et al. 2024; Hu et al. 2024b; Kocabas et al. 2024). Human Gaussian Splatting (Moreau et al. 2024) showcase 3DGS as an efficient alternative to NeRF. Splattin-gavatar (Shao et al. 2024) and Gomavatar (Wen et al. 2024) extends lifted optimization to simultaneously optimize the parameters of the Gaussians while walking on the triangle mesh. While these methods have made significant progress, they often overlook the crucial role of semantic information. It is a key focus of our **SG-GS**.

Preliminaries

SMPL (Loper et al. 2015). The SMPL model is a widely-used parametric 3D human body model that efficiently represents body shape and pose variations. In our work, We utilize SMPL’s Linear Blend Skinning (LBS) algorithm to transform points from canonical space to observation space, enabling accurate body deformation across different poses. We also leverage SMPL’s body priors for semantic information, enhancing our model’s understanding of body structure and part relationships. This semantic information is crucial for improving the quality and consistency of our human avatar reconstruction.

3D Gaussian Splatting (3DGS) (Kerbl et al. 2023). 3DGS explicitly represents scenes using point clouds, where each point is modeled as a 3D Gaussian defined by a covariance matrix Σ and a center point \mathcal{X} , the latter referred to as the mean. The value at point \mathcal{X} is:

$$G(\mathcal{X}) = e^{-\frac{1}{2}\mathcal{X}^T\Sigma^{-1}\mathcal{X}}. \quad (1)$$

For differentiable optimization, the covariance matrix Σ is decomposed into a scaling matrix \mathcal{S} and a rotation matrix \mathcal{R} , such that $\Sigma = \mathcal{R}\mathcal{S}\mathcal{S}^T\mathcal{R}^T$. In practice, \mathcal{S} and \mathcal{R} are also represented by the diagonal vector $s \in \mathbb{R}^{N \times 3}$ and a quaternion vector $r \in \mathbb{R}^{N \times 4}$, respectively. In rendering novel views, differential splatting, as introduced by (Yifan et al. 2019) and (Zwicker et al. 2001), involves applying a viewing transformation W along with the Jacobian matrix J of the affine approximation of the projective transformation. This process computes the transformed covariance matrix as: $\Sigma' = JW\Sigma W^T J^T$. The color and opacity at each pixel are computed from the Gaussian’s representation $G(\mathcal{X}) = e^{-\frac{1}{2}\mathcal{X}^T\Sigma^{-1}\mathcal{X}}$. The blending of N ordered points

overlapping a pixel is given by the formula:

$$\mathcal{C} = \sum_{i \in N} c_i \alpha_i \prod_{j=1}^{i-1} (1 - \alpha_j). \quad (2)$$

Here, c_i , α_i represents the density and color of this point computed by a 3D Gaussian G with covariance Σ multiplied by an optimizable per-point opacity and SH color coefficients. The 3D Gaussians are optimized using a photometric loss. 3DGS adjusts their number through periodic densification and pruning, achieving an optimal density distribution that accurately represents the scene.

Method

In this section, we illustrate the pipeline of our **SG-GS** in Fig. 1. The inputs to our method include images $X = \{x_i\}_{i=1}^N$ obtained from monocular videos, fitted SMPL parameters $P = \{p_i\}_{i=1}^N$, and paired foreground masks $M = \{m_i\}_{i=1}^N$ of images. **SG-GS** optimizes 3D Gaussians in canonical space, which are then deformed to match the observation space and rendered from the provided camera view. To integrate semantic information about body parts into the 3D Gaussian optimization process, we divide the human body into 5 distinct parts and represent the labels using one-hot encoding, stored as semantic attribute $\mathcal{O} \in \mathbb{R}^{10}$.

Non-rigid and Rigid Deformation

Inspired by (Weng et al. 2022; Qian et al. 2024), We decompose human deformation into two key components: 1) a non-rigid element capturing pose-dependent cloth dynamics, and 2) a rigid transformation governed by the human skeletal structure.

We employ a non-rigid deformation network, that takes the canonical position \mathcal{X}_c of the 3D Gaussians \mathcal{G}_c in canonical space and a pose latent code as input. This pose latent code encodes SMPL parameters p_i using a lightweight hierarchical pose encoder (Mihajlovic et al. 2021). The network then outputs offsets for various parameters of \mathcal{G}_c :

$$\Delta(\mathcal{X}, \mathcal{C}, \alpha, s, r) = f_{\theta_{nr}}(\mathcal{X}_c; \mathcal{Z}_p). \quad (3)$$

This network enables efficient and detailed non-rigid deformation of the 3D Gaussians, effectively capturing the nuances of human body movement and shape. The canonical Gaussian is deformed by:

$$\mathcal{X}_d = \mathcal{X}_c + \Delta\mathcal{X}, \mathcal{C}_d = \mathcal{C}_c + \Delta\mathcal{C}, \quad (4)$$

$$\alpha_d = \alpha_c + \Delta\alpha, s_d = s_c + \Delta s, \quad (5)$$

$$r_d = r_c \cdot [1, \Delta r_1, \Delta r_2, \Delta r_3], \quad (6)$$

where the quaternion multiplication \cdot is equivalent to multiplying the corresponding rotation matrices. With $[1, 0, 0, 0]$ representing the identity rotation, $r_d = r_c$ when $\delta r = \mathbf{0}$, preserving the original orientation for zero rotation offset.

We further employ a rigid deformation network to transform the non-rigidly deformed 3D Gaussians \mathcal{G}_d to the observation space \mathcal{G}_o . This is achieved via forward Linear

Blend Skinning (LBS):

$$\mathbf{T} = \sum_{b=1}^B f_{\theta_r}(\mathcal{X}_d)_b \mathbf{B}_b, \mathcal{X}_o = \mathbf{T} \mathcal{X}_d, \quad (7)$$

$$\mathcal{R}_o = \mathbf{T}_{1:3,1:3} \mathcal{R}_d, \quad (8)$$

where \mathcal{R}_d is the rotation matrix derived from quaternion r_d , and \mathbf{B}_b represents the differentiable bone transformations. This step aligns the deformed Gaussians with the target pose in the observation space \mathcal{G}_o .

Semantic Human-Body Annotator

Most current animatable human avatar creation methods just use SMPL (Loper et al. 2015) model for its pose-aware shape priors, neglecting its inherent semantic information. We argue that accurate semantic information can improve rendering quality, and we will further demonstrate this in the experimental section.

To achieve this, we deform the standard human body model from the SMPL model using the differentiable bone transformations \mathbf{B}_b as described in Eq. 7. Then, we use a custom point rasterizing function to render the deformed 3D SMPL model into an image m_i^p with a projection matrix from the dataset.

For each pixel in a foreground mask m_i , we employ the k-nearest neighbors (KNN) algorithm to identify the closest pixels in m_i^p . This process enables semantic-level annotation of body parts by transferring semantic labels from the SMPL model to the foreground mask m_i . The result is a semantically annotated mask m_i^s that accurately represents the different regions of the human body. We formalize this Semantic Human Annotation (SHA) process as follows:

$$m_i^s = \mathcal{SHA}(m_i, \mathbf{B}_b), \quad (9)$$

where \mathcal{SHA} denotes our Semantic Human-Body Annotator. We use the generated human body semantic labels m_s to ensure the accuracy of Gaussian’s semantic attribute. (described in semantic projection with 2D regularization).

Geometric and Semantic Feature Learning

Maintaining motion consistency across local neighborhoods is essential in modeling non-rigid deformation. However, point-level MLPs are limited by a small receptive field, which restricts their capability to capture the local geometric and semantic features of point clouds. To address this, we propose a 3D geometry- and semantic-aware network that effectively captures the human body’s local geometric and semantic structure in canonical space.

We employ sparse convolution (Graham and Van der Maaten 2017) on sparse voxels to extract local geometric and semantic features across varying receptive fields, following the method outlined in (Lu et al. 2024). Given the position \mathcal{X}_c of the Gaussians \mathcal{G}_c as a point cloud, we initially convert it into voxels by partitioning the space using a fixed grid size v .

$$\mathbf{V} = \lfloor \mathcal{X}_c / v \rfloor, \quad (10)$$

where $\mathbf{V} \in \mathbb{R}^{M \times 3}$ and M is the number of voxels. We then construct a 3D sparse U-Net by stacking a series of sparse

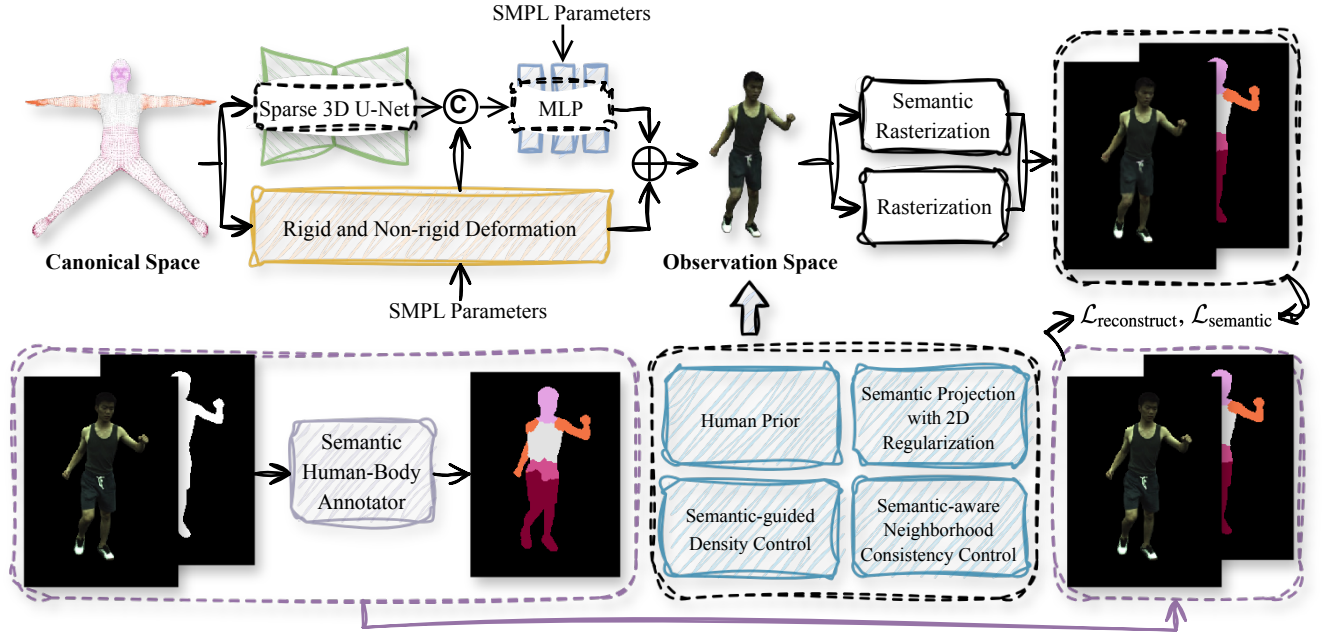


Figure 1: **Our framework for creating photo-realistic animatable avatars from monocular videos.** We initialize a set of 3D Gaussians in the canonical space by sampling 6,890 points from the SMPL model and assign the semantic attributes of Gaussians to each point. We first integrate a skeleton-driven rigid deformation and a non-rigid cloth dynamics deformation to deform human avatars from canonical space \mathcal{G}_c to observation space \mathcal{G}_o . Then, we introduce a Semantic Human-Body Annotator (SHA), which leverages SMPL’s human body semantic prior for efficient semantic labeling. These labels are used to guide the optimization of 3D Gaussian’s semantic attribute \mathcal{O} . To utilize 3D geometric and semantic information effectively, we also propose a 3D geometry- and semantic-aware network to learn body geometric and semantic associations and integrate them into learning the 3D deformation. To enhance semantic accuracy and render quality, we implement semantic projection with 2D regularization, semantic-guided density regularization and semantic-aware regularization with neighborhood consistency.

convolutions with skip connections to aggregate local features. The sparse 3D U-Net takes \mathbf{V} as input, denoted as $\mathbf{F}_v \in \mathbb{R}^{M \times C}$, where C is the feature dimension.

To fuse the geometric and semantic information, we concatenate the voxel-based features \mathbf{F}_v with the semantic point-based features \mathcal{O} , and then process them through an MLP layer:

$$\Delta(\mathcal{X}', s', r') = \text{MLP}(\text{Concat}(\mathbf{F}_v, \mathcal{O})), \quad (11)$$

where $\Delta(\mathcal{X}', s', r')$ represents the final fused features. The deformed 3D Gaussian \mathcal{G}_o is then deformed by $\Delta(\mathcal{X}', s', r')$ following Eq. 4, 5, and 6.

Optimization

During densification, newly created 3D Gaussian points inherit semantic attributes from their parent nodes.

Semantic projection with 2D regularization. We acquire rendered per-pixel semantic labels using the efficient Gaussian splatting algorithm following Eq. 2 as:

$$\mathcal{S} = \sum_{p \in \mathcal{N}} y_p \alpha_p \prod_{j=1}^{p-1} (1 - \alpha_j), \quad (12)$$

where \mathcal{S}_k represents the 2D semantic labels of pixel k , derived from Gaussian point semantic attributes via α -blending (Eq. 2). Here, y_p denotes the semantic attribute of the 3D Gaussian point p , and α_p is the influence factor of this point in rendering pixels. Upon calculating these labels, we obtain the results l_i^s and apply a BCE loss to regularize the rendered semantic label l_i^s with semantic labels generated via SHA as follows:

$$\mathcal{L}_{semantic} = \mathcal{L}_{bce}(l_i^s, m_i^s). \quad (13)$$

Semantic-guided density regularization. Fuzzy geometric shapes often appear in local structures on the human surface, particularly in high-frequency areas like clothing wrinkles and muscle textures (Wang et al. 2024). To improve the clarity and distribution of 3D Gaussians in these regions, we propose semantic-guided density regularization. We identify high-frequency nodes by assessing the average magnitude of structural differences between a selected node and all nodes within the same cluster. Nodes exhibiting the highest average magnitude of these differences are designated as high-

frequency nodes.

$$H_m = \arg \max_{i \in C_m} \left\{ \frac{1}{|C_m| - 1} \sum_{j \in C_m \setminus \{i\}} d(A_i, A_j) \right\}, \quad (14)$$

where H_m is the high-frequency node in cluster C_m , A_i is the basic attribute of 3D Gaussian points (color, opacity, etc.), C_m represents the set of all points with semantic attribute m , and $d(\cdot, \cdot)$ is a dissimilarity measure between two points. To better capture and express these local structures of significant discrepancies, we perform densification operations on these 3D Gaussians, enhancing the local rendering granularity to focus on guiding the split and attribute optimization of Gaussian points in these areas.

Semantic-aware regularization with neighborhood consistency. We expect Gaussians that are in close proximity to exhibit similar semantic attributes, thereby achieving local semantic consistency in 3D space. The loss function for this semantic consistency constraint is as follows:

$$\mathcal{L}_{neighborhood} = \frac{1}{|N|} \sum_{m \in N} \sum_{n \in N_k(m)} D_{KL}(p_m || p_n), \quad (15)$$

where N represents the total number of Gaussian points, $N_k(m)$ contains the k nearest neighbors of 3D Gaussian point m in 3D space, p_m and p_n represent the predicted probability distributions for point m and its neighbor n , respectively, and $D_{KL}(p_m || p_n)$ calculates the KL divergence between the predicted distributions of point m and its neighbor n .

Loss function. Our full loss function consists of a RGB loss \mathcal{L}_{rgb} , a mask loss \mathcal{L}_{mask} , a skinning weight regularization loss \mathcal{L}_{skin} , the as-isometric-as-possible regularization loss \mathcal{L}_{isopos} following (Qian et al. 2024), Semantic projection with 2D regularization $\mathcal{L}_{semantic}$, and Semantic-aware regularization with neighborhood consistency $\mathcal{L}_{neighborhood}$:

$$\mathcal{L}_{reconstruct} = \mathcal{L}_{rgb} + \lambda_1 \mathcal{L}_{mask} + \lambda_2 \mathcal{L}_{SSIM} + \lambda_3 \mathcal{L}_{LPIPS} + \lambda_4 \mathcal{L}_{skin} + \lambda_5 \mathcal{L}_{isopos}. \quad (16)$$

The final loss function is:

$$\mathcal{L} = \mathcal{L}_{reconstruct} + \lambda_6 \mathcal{L}_{semantic} + \lambda_7 \mathcal{L}_{neighborhood}, \quad (17)$$

where λ 's are loss weights. For further details of the loss definition and respective weights, please refer to the Supp.Mat.

Experiment

In this section, we first compare **SG-GS** with recent SOTA methods (Peng et al. 2021b,a; Weng et al. 2022; Wang et al. 2022c; Yu et al. 2023; Qian et al. 2024; Hu et al. 2024b,a), demonstrating that our **SG-GS** achieves superior rendering quality. We then systematically ablate each component of the proposed method, showing their effectiveness in better rendering performance. All models are trained on one single NVIDIA RTX 3090 GPU. For further details of implementation, please refer to the Supp.Mat.

Table 1: **Quantitative Results on ZJU-MoCap (Peng et al. 2021b).** **SG-GS** achieves state-of-the-art performance across every method. The **best** and the **second best** results are denoted by pink and yellow. Frames per second (FPS) is measured on an RTX 3090. LPIPS* = LPIPS \times 1000.

Method:	PSNR \uparrow	SSIM \uparrow	LPIPS* \downarrow	FPS
NeuralBody (Peng et al. 2021b)	29.07	0.962	52.29	1.5
Ani-NeRF (Peng et al. 2021a)	29.17	0.961	51.98	1.1
HumanNeRF (Weng et al. 2022)	30.24	0.968	31.73	0.3
MonoHuman (Yu et al. 2023)	29.38	0.964	37.51	0.1
InstantAvatar (Jiang et al. 2023)	29.73	0.938	64.41	4.2
3DGS-Avatar (Qian et al. 2024)	30.62	0.965	30.28	50
GauHuman (Hu et al. 2024b)	30.79	0.960	32.73	180
GoMAvatar (Wen et al. 2024)	30.37	0.969	32.53	43
SG-GS	30.88	0.969	29.69	25

Table 2: **Quantitative Results on H36M (Ionescu et al. 2013).**

Method:	Training Poses		Novel Poses	
	PSNR \uparrow	SSIM \uparrow	PSNR \uparrow	SSIM \uparrow
NARF (Noguchi et al. 2021)	23.00	0.898	22.27	0.881
NeuralBody (Peng et al. 2021b)	22.89	0.896	23.09	0.891
Ani-NeRF (Peng et al. 2021a)	23.00	0.890	22.55	0.880
ARAH (Wang et al. 2022c)	24.79	0.918	23.42	0.896
3DGS-Avatar (Qian et al. 2024)	32.89	0.982	32.50	0.983
SG-GS	33.01	0.989	33.14	0.987

Dataset

ZJU-MoCap (Peng et al. 2021b). It records multi-view videos with 21 cameras and collects human poses using the marker-less motion capture system. We select six sequences (377, 386, 387, 392, 393, 394) from this dataset to conduct experiments. We also follow the same training/test split as HumanNeRF (Weng et al. 2022) and 3DGS-Avatar (Qian et al. 2024), *i.e.*, one camera is used for training, while the remaining cameras are used for evaluation.

H36M (Ionescu et al. 2013). It captures multi-view videos using four cameras and collects human poses with a marker-based motion capture system. It includes multiple subjects performing complex actions. We select representative actions, split the videos into training and test frames, following ARAH (Wang et al. 2022c), and perform experiments on sequences (S1, S5, S6, S7, S8, S9, S11). Three cameras are used for training and the remaining is selected for test.

Comparison with State-of-the-art Methods

We conduct comparative experiments against various state-of-the-art (SOTA) methods for human avatars, including NeRF-based methods such as NeuralBody (Peng et al. 2021b), Ani-NeRF (Peng et al. 2021a), HumanNeRF (Weng et al. 2022), and MonoHuman (Yu et al. 2023), as well as 3DGS-based methods such as 3DGS-Avatar (Qian et al. 2024), GauHuman (Hu et al. 2024b), and GoMAvatar (Wen et al. 2024), under a monocular setup on ZJU-MoCap (Peng

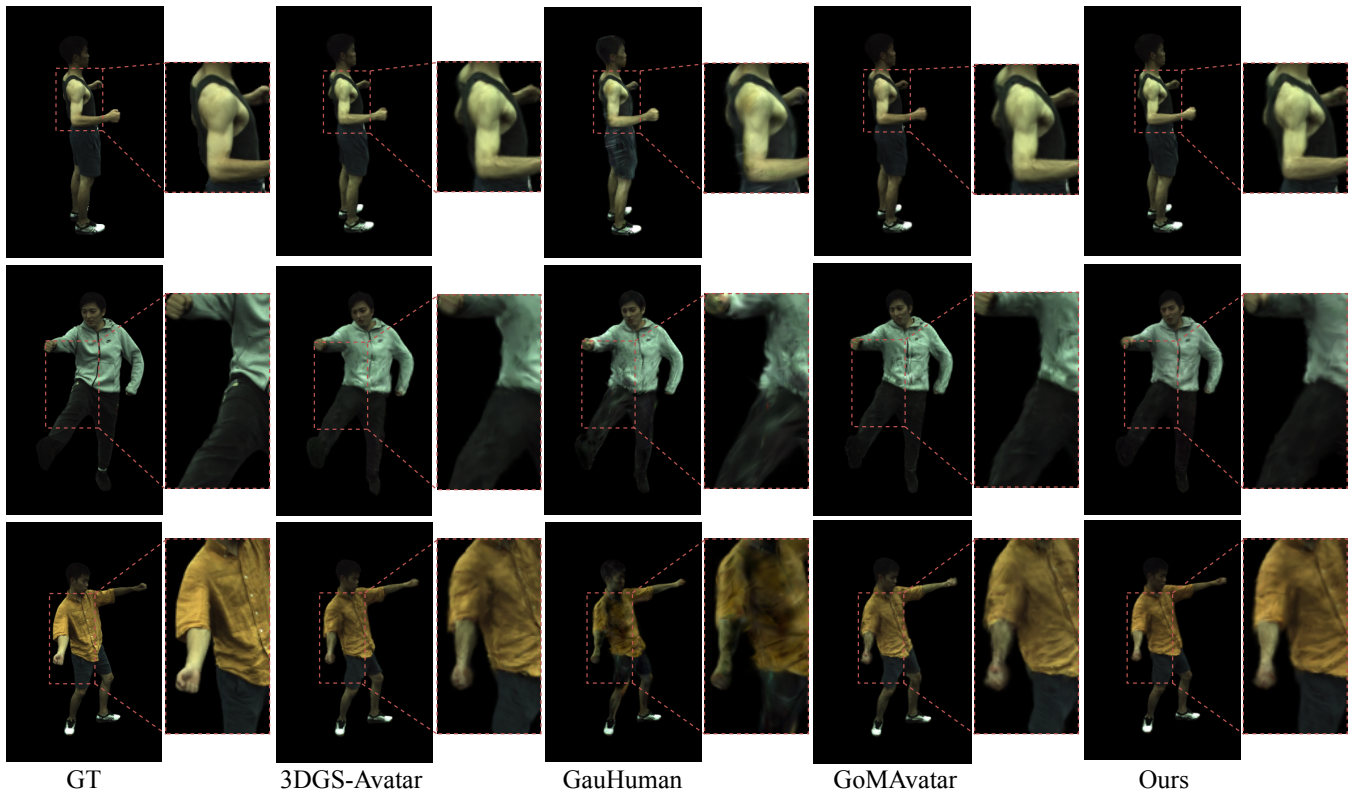


Figure 2: **Qualitative Comparison on ZJU-MoCap (Peng et al. 2021b)**. We show that our **SG-GS** can produce realistic details in both rendered images and geometry, while other approaches struggle to generate smooth details.

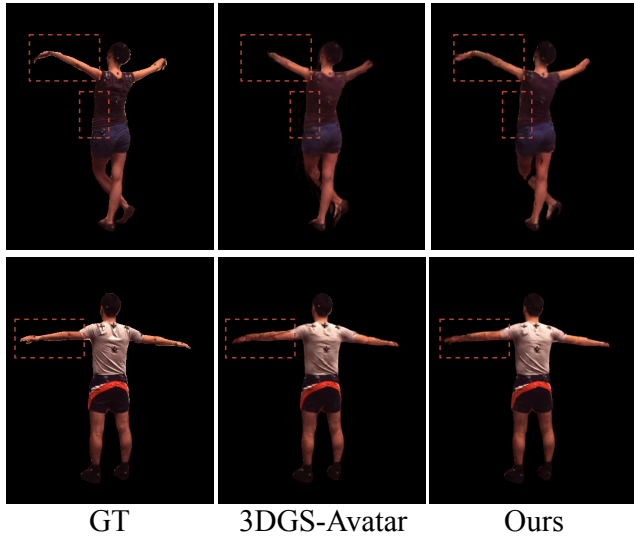


Figure 3: **Qualitative Comparison on H36M (Ionescu et al. 2013)**. By utilizing semantic information within human body, our **SG-GS** preserves better anatomical structures of the human body, producing high-quality results

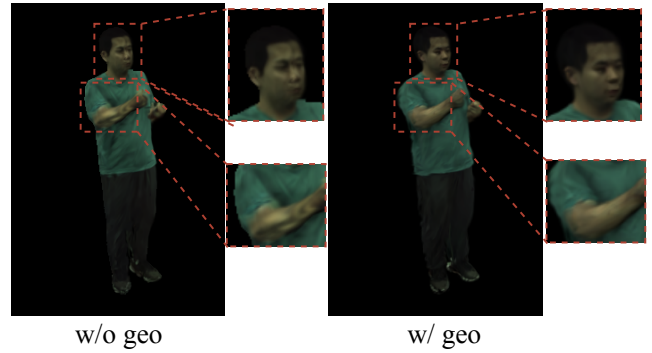


Figure 4: **Ablation Study** on Geometric and Semantic Feature Learning, which helps erase artifacts and learn fine details like cloth wrinkles and human face.

et al. 2021b). In Tab.1, we evaluate the reconstruction quality using three different metrics: PSNR, SSIM, and LPIPS. Thanks to the LBS weight field and deformation field learned in HumanNeRF(Weng et al. 2022), 3DGS-Avatar (Qian et al. 2024), and GauHuman (Hu et al. 2024b), these methods achieve comparable visualization results. In comparison, our proposed **SG-GS** achieves good perfor-

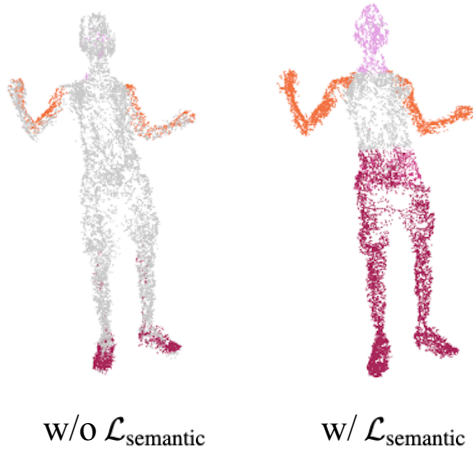


Figure 5: **Ablation Study** on semantic projection with 2D regularization, which enhances semantic accuracy.

mance in terms of PSNR and SSIM while significantly outperforming existing methods on LPIPS. **Existing researches (Park et al. 2021; Yang et al. 2024a) have reached a consensus that LPIPS provides more meaningful insights compared to the other metrics, given the challenges of reproducing exact ground-truth appearances for novel views.**

As shown in Fig. 2, our **SG-GS** method preserves sharper details compared to other methods. **Notably, our approach excels at capturing fine details in challenging areas such as clothing, where reconstruction is typically more difficult due to intricate textures.** By preserving these finer details, our method provides a more realistic and detailed reconstruction of clothing and other complex surfaces, significantly improving the overall quality and fidelity of the 3D human avatars.

In addition, we also evaluate our **SG-GS** using the H36M (Ionescu et al. 2013) dataset. We report the quantitative results against NeRF-based methods such as NARF (Noguchi et al. 2021), NeuralBody (Peng et al. 2021b), Ani-NeRF (Peng et al. 2021a), and ARAH (Wang et al. 2022c), as well as 3DGS-based methods such as 3DGS-Avatar (Qian et al. 2024) in Tab.2. Our model outperforms both established NeRF-based methods and 3DGS-based methods.

As shown in Fig.3, due to the use of semantic information within human body, our **SG-GS** achieves better reconstruction of edge areas and preserves anatomical structures of the human body.

Ablation Study

In this section, we evaluate the effectiveness of our proposed modules through ablation experiments on the ZJU-MoCap dataset. These modules include Geometric and Semantic Feature Learning (geo), semantic projection with 2D regu-

Table 3: **Ablation Study on ZJU-MoCap (Peng et al. 2021b).** The proposed model achieves the lowest LPIPS, demonstrating the effectiveness of all components.

Method:	PSNR \uparrow	SSIM \uparrow	LPIPS* \downarrow	FPS
Baseline	30.17	0.961	36.57	70
w/o geo	30.64	0.970	32.75	70
w/o $\mathcal{L}_{semantic}$	30.67	0.966	29.99	25
w/o sgd	30.55	0.968	31.01	25
w/o $\mathcal{L}_{neighborhood}$	30.56	0.965	30.59	25
SG-GS	30.88	0.969	29.69	25

larization ($\mathcal{L}_{semantic}$), semantic-guided density regularization (sgd), and semantic-aware regularization with Neighborhood Consistency ($\mathcal{L}_{neighborhood}$). The average metrics over 6 sequences are shown in Table 3.

Geometric and Semantic Feature Learning. This module is designed to learn the associations between body geometry and semantics for 3D deformation. As shown in Table 3, it significantly enhances rendering performance. Though it slightly increase inference time, the notable performance improvement justifies this additional cost. A qualitative comparison in Fig. 4 further proves that Geometric and Semantic Feature Learning reduces artifacts and captures fine details like cloth wrinkles and facial features.

Semantic Projection with 2D Regularization. This part utilizes semantic labels generated by SHA to supervise the semantic attributes of 3D Gaussians. As shown in Fig. 5, semantic projection with 2D regularization substantially improves the semantic accuracy of 3D Gaussians. The results in Table 3 illustrate the critical role of semantic information in creating photo-realistic animatable human avatars.

Semantic-Guided Density Regularization and Semantic-Aware Regularization with Neighborhood Consistency. Semantic-guided density regularization enhances rendering quality by optimizing Gaussian density in areas with high discrepancy, while semantic-aware regularization with neighborhood consistency ensures that nearby Gaussians exhibit coherent semantic attributes, thus improving 3D semantic consistency. The improvements in rendering quality are validated by the results in Table 3.

Conclusion

In this paper, we propose SG-GS, which uses semantics-embedded 3D Gaussians to reconstruct photo-realistic animatable human avatars. SG-GS first integrates a skeleton-driven rigid deformation and a non-rigid cloth dynamics deformation to deform photo-realistic animatable human avatars. SG-GS then leverages SMPL’s human body semantic priors to acquire human body semantic labels, which are used to guide optimization of Gaussian’s semantic attribute. To utilize local geometric and semantic information effectively, we propose a 3D geometry- and semantic-aware network to learn body geometric and semantic associations and integrate them into the 3D deformation. We further implement three key strategies to enhance semantic accuracy and render quality: semantic projection with

2D regularization, semantic-guided density regularization, and semantic-aware regularization with neighborhood consistency. Extensive experiments demonstrate that **SG-GS** outperforms SOTA methods in creating photo-realistic animatable avatars, further validating our hypothesis that integrating semantic priors enhances fine-detail reconstruction. We hope that our method will foster further research in high-quality clothed human avatar synthesis from monocular views.

Limitations. 1). **SG-GS** lacks the capability to extract 3D meshes. Developing a method to extract meshes from 3D Gaussians is an important direction for future research. 2). Geometric and Semantic Feature Learning employs a 3D sparse U-Net, which is computationally intensive and may increase training and inference time to some extent.

References

- Chen, A.; Xu, Z.; Geiger, A.; Yu, J.; and Su, H. 2022. Tensorf: Tensorial radiance fields. In *Proc. of European Conf. on Computer Vision*, 333–350.
- Chen, Y.; Wang, X.; Chen, X.; Zhang, Q.; Li, X.; Guo, Y.; Wang, J.; and Wang, F. 2023. Uv volumes for real-time rendering of editable free-view human performance. In *Proc. of IEEE Conf. on Computer Vision and Pattern Recognition*, 16621–16631.
- Fridovich-Keil, S.; Yu, A.; Tancik, M.; Chen, Q.; Recht, B.; and Kanazawa, A. 2022. Plenoxels: Radiance fields without neural networks. In *Proc. of IEEE Conf. on Computer Vision and Pattern Recognition*, 5501–5510.
- Graham, B.; and Van der Maaten, L. 2017. Submanifold sparse convolutional networks. *arXiv preprint arXiv:1706.01307*.
- Guo, C.; Jiang, T.; Chen, X.; Song, J.; and Hilliges, O. 2023. Vid2avatar: 3d avatar reconstruction from videos in the wild via self-supervised scene decomposition. In *Proc. of IEEE Conf. on Computer Vision and Pattern Recognition*, 12858–12868.
- Healey, J.; Wang, D.; Wigington, C.; Sun, T.; and Peng, H. 2021. A mixed-reality system to promote child engagement in remote intergenerational storytelling. In *IEEE International Symposium on Mixed and Augmented Reality Adjunct (ISMAR-Adjunct)*, 274–279.
- Ho, H.-I.; Xue, L.; Song, J.; and Hilliges, O. 2023. Learning locally editable virtual humans. In *Proc. of IEEE Conf. on Computer Vision and Pattern Recognition*, 21024–21035.
- Hu, L.; Zhang, H.; Zhang, Y.; Zhou, B.; Liu, B.; Zhang, S.; and Nie, L. 2024a. Gaussianavatar: Towards realistic human avatar modeling from a single video via animatable 3d gaussians. In *Proc. of IEEE Conf. on Computer Vision and Pattern Recognition*, 634–644.
- Hu, S.; et al. 2024b. GauHuman: Articulated gaussian splatting from monocular human videos. In *cvpr*, 20418–20431.
- Ionescu, C.; Papava, D.; Olaru, V.; and Sminchisescu, C. 2013. Human3.6m: Large scale datasets and predictive methods for 3d human sensing in natural environments. *IEEE Trans. on Pattern Anal. and Mach. Intell.*, 36(7): 1325–1339.
- Jiang, T.; Chen, X.; Song, J.; and Hilliges, O. 2023. InstantAvatar: Learning Avatars from Monocular Video in 60 Seconds. In *Proc. of IEEE Conf. on Computer Vision and Pattern Recognition*, 16922–16932.
- Jiang, W.; Yi, K. M.; Samei, G.; Tuzel, O.; and Ranjan, A. 2022. Neuman: Neural human radiance field from a single video. In *Proc. of European Conf. on Computer Vision*, 402–418. Springer.
- Jiang, Y.; Shen, Z.; Wang, P.; Su, Z.; Hong, Y.; Zhang, Y.; Yu, J.; and Xu, L. 2024. HiFi4G: High-fidelity human performance rendering via compact gaussian splatting. In *Proc. of IEEE Conf. on Computer Vision and Pattern Recognition*, 19734–19745.
- Kerbl, B.; Kopanas, G.; Leimkühler, T.; and Drettakis, G. 2023. 3d gaussian splatting for real-time radiance field rendering. *ACM Transactions on Graphics*, 42(4): 1–14.
- Kocabas, M.; Chang, J.-H. R.; Gabriel, J.; Tuzel, O.; and Ranjan, A. 2024. HUGS: Human gaussian splats. In *Proc. of IEEE Conf. on Computer Vision and Pattern Recognition*, 505–515.
- Lei, J.; Wang, Y.; Pavlakos, G.; Liu, L.; and Daniilidis, K. 2024. GART: Gaussian articulated template models. In *Proc. of IEEE Conf. on Computer Vision and Pattern Recognition*, 19876–19887.
- Li, R.; Tanke, J.; Vo, M.; Zollhöfer, M.; Gall, J.; Kanazawa, A.; and Lassner, C. 2022. TAVA: Template-free animatable volumetric actors. In *Proc. of European Conf. on Computer Vision*, 419–436.
- Li, Z.; Zheng, Z.; Liu, Y.; Zhou, B.; and Liu, Y. 2023. Posevocab: Learning joint-structured pose embeddings for human avatar modeling. In *ACM SIGGRAPH 2023 Conference Proceedings*, 1–11.
- Liu, L.; Habermann, M.; Rudnev, V.; Sarkar, K.; Gu, J.; and Theobalt, C. 2021. Neural actor: Neural free-view synthesis of human actors with pose control. *ACM transactions on graphics (TOG)*, 40(6): 1–16.
- Loper, M.; Mahmood, N.; Romero, J.; Pons-Moll, G.; and Black, M. J. 2015. SMPL: A Skinned Multi-Person Linear Model. *Acm Transactions on Graphics*, 34(248).
- Lu, Z.; Guo, X.; Hui, L.; Chen, T.; Yang, M.; Tang, X.; Zhu, F.; and Dai, Y. 2024. 3d geometry-aware deformable gaussian splatting for dynamic view synthesis. In *Proc. of IEEE Conf. on Computer Vision and Pattern Recognition*, 8900–8910.
- Luiten, J.; Kopanas, G.; Leibe, B.; and Ramanan, D. 2024. Dynamic 3d gaussians: Tracking by persistent dynamic view synthesis. In *3DV*.
- Mihajlovic, M.; Zhang, Y.; Black, M. J.; and Tang, S. 2021. LEAP: Learning articulated occupancy of people. In *Proc. of IEEE Conf. on Computer Vision and Pattern Recognition*, 10461–10471.
- Mildenhall, B.; Srinivasan, P. P.; Tancik, M.; Barron, J. T.; Ramamoorthi, R.; and Ng, R. 2021. Nerf: Representing scenes as neural radiance fields for view synthesis. *Communications of the ACM*, 65(1): 99–106.

- Moreau, A.; Song, J.; Dharmo, H.; Shaw, R.; Zhou, Y.; and Pérez-Pellitero, E. 2024. Human gaussian splatting: Real-time rendering of animatable avatars. In *Proc. of IEEE Conf. on Computer Vision and Pattern Recognition*, 788–798.
- Müller, T.; Evans, A.; Schied, C.; and Keller, A. 2022. Instant neural graphics primitives with a multiresolution hash encoding. *ACM transactions on graphics (TOG)*, 41(4): 1–15.
- Niemeyer, M.; Mescheder, L.; Oechsle, M.; and Geiger, A. 2020. Differentiable volumetric rendering: Learning implicit 3d representations without 3d supervision. In *Proc. of IEEE Conf. on Computer Vision and Pattern Recognition*, 3504–3515.
- Noguchi, A.; Sun, X.; Lin, S.; and Harada, T. 2021. Neural articulated radiance field. In *Proc. of IEEE Intl. Conf. on Computer Vision*, 5762–5772.
- Oechsle, M.; Peng, S.; and Geiger, A. 2021. Unisurf: Unifying neural implicit surfaces and radiance fields for multi-view reconstruction. In *Proc. of IEEE Intl. Conf. on Computer Vision*, 5589–5599.
- Park, K.; Sinha, U.; Hedman, P.; Barron, J. T.; Bouaziz, S.; Goldman, D. B.; Martin-Brualla, R.; and Seitz, S. M. 2021. Hypernerf: A higher-dimensional representation for topologically varying neural radiance fields. *arXiv preprint arXiv:2106.13228*.
- Peng, S.; Dong, J.; Wang, Q.; Zhang, S.; Shuai, Q.; Zhou, X.; and Bao, H. 2021a. Animatable neural radiance fields for modeling dynamic human bodies. In *Proc. of IEEE Intl. Conf. on Computer Vision*, 14314–14323.
- Peng, S.; Zhang, Y.; Xu, Y.; Wang, Q.; Shuai, Q.; Bao, H.; and Zhou, X. 2021b. Neural Body: Implicit Neural Representations with Structured Latent Codes for Novel View Synthesis of Dynamic Humans. In *Proc. of IEEE Conf. on Computer Vision and Pattern Recognition*, 9054–9063.
- Qian, Z.; Wang, S.; Mihajlovic, M.; Geiger, A.; and Tang, S. 2024. 3dgs-avatar: Animatable avatars via deformable 3d gaussian splatting. In *Proc. of IEEE Conf. on Computer Vision and Pattern Recognition*, 5020–5030.
- Raj, A.; Tanke, J.; Hays, J.; Vo, M.; Stoll, C.; and Lassner, C. 2021. Anr: Articulated neural rendering for virtual avatars. In *Proc. of IEEE Conf. on Computer Vision and Pattern Recognition*, 3722–3731.
- Reiser, C.; Peng, S.; Liao, Y.; and Geiger, A. 2021. Kilonerf: Speeding up neural radiance fields with thousands of tiny mlps. In *Proc. of IEEE Conf. on Computer Vision and Pattern Recognition*, 14335–14345.
- Rückert, D.; Franke, L.; and Stamminger, M. 2022. Adop: Approximate differentiable one-pixel point rendering. *ACM Transactions on Graphics (ToG)*, 41(4): 1–14.
- Shao, Z.; Wang, Z.; Li, Z.; Wang, D.; Lin, X.; Zhang, Y.; Fan, M.; and Wang, Z. 2024. Splattingavatar: Realistic real-time human avatars with mesh-embedded gaussian splatting. In *Proc. of IEEE Conf. on Computer Vision and Pattern Recognition*, 1606–1616.
- Sitzmann, V.; Rezkhanov, S.; Freeman, B.; Tenenbaum, J.; and Durand, F. 2021. Light field networks: Neural scene representations with single-evaluation rendering. *Proc. of Advances in Neural Information Processing Systems*, 34: 19313–19325.
- Su, S.-Y.; Bagautdinov, T.; and Rhodin, H. 2023. NPC: Neural point characters from video. In *Proc. of IEEE Intl. Conf. on Computer Vision*, 14795–14805.
- Wang, H.; Ren, J.; Huang, Z.; Olszewski, K.; Chai, M.; Fu, Y.; and Tulyakov, S. 2022a. R2l: Distilling neural radiance field to neural light field for efficient novel view synthesis. In *Proc. of European Conf. on Computer Vision*, 612–629. Springer.
- Wang, H.; Zhang, W.; Liu, S.; Zhou, X.; Zhang, S.; Wu, F.; and Lin, F. 2024. Gaussian Control with Hierarchical Semantic Graphs in 3D Human Recovery. *arXiv preprint arXiv:2405.12477*.
- Wang, S.; Schwarz, K.; Geiger, A.; and Tang, S. 2022b. Arah: Animatable volume rendering of articulated human sdfs. In *Proc. of European Conf. on Computer Vision*, 1–19. Springer.
- Wang, S.; Schwarz, K.; Geiger, A.; and Tang, S. 2022c. ARAH: Animatable Volume Rendering of Articulated Human SDFs. In *Proc. of European Conf. on Computer Vision*, 1–19.
- Wen, J.; Zhao, X.; Ren, Z.; Schwing, A. G.; and Wang, S. 2024. GoMAvatar: Efficient animatable human modeling from monocular video using gaussians-on-mesh. In *Proceedings of the IEEE/CVF Conference on Computer Vision and Pattern Recognition*, 2059–2069.
- Weng, C.-Y.; Curless, B.; Srinivasan, P. P.; Barron, J. T.; and Kemelmacher-Shlizerman, I. 2022. HumanNeRF: Free-viewpoint Rendering of Moving People from Monocular Video. In *Proc. of IEEE Conf. on Computer Vision and Pattern Recognition*, 16210–16220.
- Wu, G.; Yi, T.; Fang, J.; Xie, L.; Zhang, X.; Wei, W.; Liu, W.; Tian, Q.; and Wang, X. 2024. 4d gaussian splatting for real-time dynamic scene rendering. In *Proc. of IEEE Conf. on Computer Vision and Pattern Recognition*, 20310–20320.
- Xu, H.; Alldieck, T.; and Sminchisescu, C. 2021. H-nerf: Neural radiance fields for rendering and temporal reconstruction of humans in motion. *Proc. of Advances in Neural Information Processing Systems*, 34: 14955–14966.
- Yang, C.; Li, S.; Fang, J.; Liang, R.; Xie, L.; Zhang, X.; Shen, W.; and Tian, Q. 2024a. Gaussianobject: Just taking four images to get a high-quality 3d object with gaussian splatting. *arXiv preprint arXiv:2402.10259*.
- Yang, Z.; Gao, X.; Zhou, W.; Jiao, S.; Zhang, Y.; and Jin, X. 2024b. Deformable 3d gaussians for high-fidelity monocular dynamic scene reconstruction. In *Proceedings of the IEEE/CVF Conference on Computer Vision and Pattern Recognition*, 20331–20341.
- Yifan, W.; Serena, F.; Wu, S.; Öztireli, C.; and Sorkine-Hornung, O. 2019. Differentiable surface splatting for point-based geometry processing. *ACM Transactions on Graphics*, 38(6): 1–14.
- Yu, Z.; Cheng, W.; Liu, x.; Wu, W.; and Lin, K.-Y. 2023. MonoHuman: Animatable Human Neural Field from

Monocular Video. In *Proc. of IEEE Conf. on Computer Vision and Pattern Recognition*, 16943–16953.

Zackariasson, P.; and Wilson, T. L. 2012. *The video game industry: Formation, present state, and future*. Routledge.

Zhao, H.; Zhao, X.; Zhu, L.; Zheng, W.; and Xu, Y. 2024. HFGS: 4D Gaussian Splatting with Emphasis on Spatial and Temporal High-Frequency Components for Endoscopic Scene Reconstruction. *arXiv preprint arXiv:2405.17872*.

Zheng, Y.; Yifan, W.; Wetzstein, G.; Black, M. J.; and Hilliges, O. 2023. Pointavatar: Deformable point-based head avatars from videos. In *Proc. of IEEE Conf. on Computer Vision and Pattern Recognition*, 21057–21067.

Zwicker, M.; Pfister, H.; Van Baar, J.; and Gross, M. 2001. Surface splatting. In *Proceedings of the 28th annual conference on Computer graphics and interactive techniques*, 371–378.

Reproducibility Checklist

This paper:

- Includes a conceptual outline and/or pseudocode description of AI methods introduced. (yes)
- Clearly delineates statements that are opinions, hypothesis, and speculation from objective facts and results. (yes)
- Provides well marked pedagogical references for less-familare readers to gain background necessary to replicate the paper. (yes)

Does this paper make theoretical contributions? (yes)

- All assumptions and restrictions are stated clearly and formally. (yes)
- All novel claims are stated formally (e.g., in theorem statements). (yes)
- Proofs of all novel claims are included. (yes)
- Proof sketches or intuitions are given for complex and/or novel results. (yes)
- Appropriate citations to theoretical tools used are given. (yes)
- All theoretical claims are demonstrated empirically to hold. (yes)
- All experimental code used to eliminate or disprove claims is included. (NA)

Does this paper rely on one or more datasets? (yes)

- A motivation is given for why the experiments are conducted on the selected datasets. (yes)
- All novel datasets introduced in this paper are included in a data appendix. (NA)
- All novel datasets introduced in this paper will be made publicly available upon publication of the paper with a license that allows free usage for research purposes. (NA)
- All datasets drawn from the existing literature (potentially including authors' own previously published work) are accompanied by appropriate citations. (yes)
- All datasets drawn from the existing literature (potentially including authors' own previously published work) are publicly available. (yes)

- All datasets that are not publicly available are described in detail, with explanation why publicly available alternatives are not scientifically satisfying. (yes)

Does this paper include computational experiments? (yes)

- Any code required for pre-processing data is included in the appendix. (yes)
- All source code required for conducting and analyzing the experiments is included in a code appendix. (no) Our code will be made available upon publication of the article.
- All source code required for conducting and analyzing the experiments will be made publicly available upon publication of the paper with a license that allows free usage for research purposes. (yes)
- All source code implementing new methods have comments detailing the implementation, with references to the paper where each step comes from. (yes)
- If an algorithm depends on randomness, then the method used for setting seeds is described in a way sufficient to allow replication of results. (yes)
- This paper specifies the computing infrastructure used for running experiments (hardware and software), including GPU/CPU models; amount of memory; operating system; names and versions of relevant software libraries and frameworks. (yes)
- This paper formally describes evaluation metrics used and explains the motivation for choosing these metrics. (yes)
- This paper states the number of algorithm runs used to compute each reported result. (yes)
- Analysis of experiments goes beyond single-dimensional summaries of performance (e.g., average; median) to include measures of variation, confidence, or other distributional information. (yes)
- The significance of any improvement or decrease in performance is judged using appropriate statistical tests (e.g., Wilcoxon signed-rank). (yes)
- This paper lists all final (hyper-)parameters used for each model/algorithm in the paper's experiments. (yes)
- This paper states the number and range of values tried per (hyper-) parameter during development of the paper, along with the criterion used for selecting the final parameter setting. (yes)

Implementation Details

We preprocess the dataset following the ARAH¹. During optimization, we follow the same strategy from (Kerbl et al. 2023) to densify and prune the 3D Gaussians, using the view-space position gradients derived from the transformed Gaussians in the observation space as the criterion for densification.

Our model is trained for a total of $15k$ iterations on the ZJU-MoCap (Peng et al. 2021b) dataset and $12k$ iterations on H36M (Ionescu et al. 2013) on a single NVIDIA RTX 3090 GPU. We use Adam to optimize our model and the per-frame latent codes with hyperparameters $\beta_1 = 0.9$ and $\beta_2 = 0.999$. The learning rate of 3D Gaussians is exactly the same as the original implementation from (Kerbl et al. 2023). We set the learning rate for forward skinning network θ_r to 1×10^{-4} , 5×10^{-4} for 3D sparse U-Net, and 1×10^{-3} for all the others. An exponential learning rate scheduler is employed to gradually decrease the learning rate by a factor of 0.1 on neural networks. We also apply a weight decay with a weight of 0.05 to the per-frame latent codes.

Following prior works (Weng et al. 2022; Qian et al. 2024), we split the training stage and learn the whole model in a coarse-to-fine manner. In the first $1k$ iterations, we freeze everything except the forward skinning network f_{θ_r} to learn a coarse skinning field with \mathcal{L}_{skin} . We then enable optimization on the 3D Gaussians after $1k$ steps. To decouple rigid and non-rigid motion, we start to optimize the non-rigid deformation network $f_{\theta_{nr}}$ after $3k$ iterations. Lastly, we turn on Geometric and Semantic Feature Learning after $5k$ iterations.

Implementation Details for Baselines

In this section, we elaborate on the implementation details of baselines used for comparison to our proposed method, *i.e.* NeuralBody (Peng et al. 2021b), HumanNeRF (Weng et al. 2022), MonoHuman (Yu et al. 2023) and InstantAvatar (Jiang et al. 2023).

For NeuralBody (Peng et al. 2021b), HumanNeRF (Weng et al. 2022), MonoHuman (Yu et al. 2023) and InstantAvatar (Jiang et al. 2023), we use the results of them reported in 3DGS-Avatar (Qian et al. 2024) which follow the same data split.

For 3DGS-Avatar (Qian et al. 2024), we train the models using the code from official code repository². For GauHuman (Hu et al. 2024b), we train the models using the code from official code repository³ for 15000 epochs. For GoMAvatar (Wen et al. 2024), we train the models using the code from official code repository⁴. All other hyperparameters remain unchanged. The trained models are then used for qualitative evaluation and out-of-distribution pose animation.

¹<https://github.com/taconite/arah-release>

²<https://github.com/mikeqzy/3dgs-avatar-release>

³<https://github.com/skhu101/GauHuman>

⁴<https://github.com/wenj/GoMAvatar>

Loss Definition

In the main paper we describe our loss term which can be formulated as follows:

$$\mathcal{L}_{reconstruct} = \mathcal{L}_{rgb} + \lambda_1 \mathcal{L}_{mask} + \lambda_2 \mathcal{L}_{SSIM} + \lambda_3 \mathcal{L}_{LPIPS} + \lambda_4 \mathcal{L}_{skin} + \lambda_5 \mathcal{L}_{isopos}, \quad (18)$$

$$\mathcal{L} = \mathcal{L}_{reconstruct} + \lambda_6 \mathcal{L}_{semantic} + \lambda_7 \mathcal{L}_{neighborhood}. \quad (19)$$

We describe how each loss term is defined below:

RGB Loss. We employ an $l1$ loss for pixel-wise error and a perceptual loss for robustness against local misalignments, crucial in monocular setups.

Mask Loss. To boost the convergence of 3D Gaussian positions, we use an explicit mask loss. For each pixel p , we compute the opacity value O_p by summing up the sample weights in the rendering equation in the main paper:

$$O_p = \sum_i \alpha'_i \prod_{j=1}^{i-1} (1 - \alpha'_j). \quad (20)$$

We thus supervise it with the ground truth foreground mask via an $l1$ loss. Experiments show that the $l1$ loss provides faster convergence than the Binary Cross Entropy (BCE) loss.

SSIM Loss. We further employ SSIM to ensure the structural similarity between ground truth target image C and synthesized images \hat{C} :

$$\mathcal{L}_{SSIM} = SSIM(\hat{C}, C). \quad (21)$$

LPIPS Loss. Following (Weng et al. 2022), we use VGG-based LPIPS as the perceptual loss. Unlike NeRF methods, we render full images via rasterization, eliminating the need for patch sampling. For efficiency, we compute LPIPS on cropped bounding boxes using ground truth masks:

$$\mathcal{L}_{LPIPS} = LPIPS(\hat{C}, C). \quad (22)$$

Skinning Loss: We leverage SMPL prior by sampling 1024 points \mathbf{X}_{skin} on the surface of the canonical SMPL mesh and regularizing the forward skinning network with corresponding skinning weights \mathbf{w} interpolated with barycentric coordinates.

$$\mathcal{L}_{skin} = \frac{1}{|\mathbf{X}_{skin}|} \sum_{\mathbf{x}_{skin} \in \mathbf{X}_{skin}} \|f_{\theta_r}(\mathbf{x}_{skin}) - \mathbf{w}\|^2. \quad (23)$$

We set $\lambda_1 = 0.5$, $\lambda_2 = 0.05$, $\lambda_3 = 0.01$, $\lambda_4 = 0.1$, $\lambda_5 = 1$, $\lambda_6 = 0.1$, $\lambda_7 = 0.1$ in all experiments. For λ_4 , we set it to 10 for the first $1k$ iterations for fast convergence to a reasonable skinning field, then decreased to 0.1 for soft regularization.

Reproducibility Checklist

This paper:

- Includes a conceptual outline and/or pseudocode description of AI methods introduced. (yes)

- Clearly delineates statements that are opinions, hypothesis, and speculation from objective facts and results. (yes)
- Provides well marked pedagogical references for less-familiar readers to gain background necessary to replicate the paper. (yes)

Does this paper make theoretical contributions? (yes)

- All assumptions and restrictions are stated clearly and formally. (yes)
- All novel claims are stated formally (e.g., in theorem statements). (yes)
- Proofs of all novel claims are included. (yes)
- Proof sketches or intuitions are given for complex and/or novel results. (yes)
- Appropriate citations to theoretical tools used are given. (yes)
- All theoretical claims are demonstrated empirically to hold. (yes)
- All experimental code used to eliminate or disprove claims is included. (NA)

Does this paper rely on one or more datasets? (yes)

- A motivation is given for why the experiments are conducted on the selected datasets. (yes)
- All novel datasets introduced in this paper are included in a data appendix. (NA)
- All novel datasets introduced in this paper will be made publicly available upon publication of the paper with a license that allows free usage for research purposes. (NA)
- All datasets drawn from the existing literature (potentially including authors' own previously published work) are accompanied by appropriate citations. (yes)
- All datasets drawn from the existing literature (potentially including authors' own previously published work) are publicly available. (yes)
- All datasets that are not publicly available are described in detail, with explanation why publicly available alternatives are not scientifically satisfying. (yes)

Does this paper include computational experiments? (yes)

- Any code required for pre-processing data is included in the appendix. (yes)
- All source code required for conducting and analyzing the experiments is included in a code appendix. (no) Our code will be made available upon publication of the article.
- All source code required for conducting and analyzing the experiments will be made publicly available upon publication of the paper with a license that allows free usage for research purposes. (yes)
- All source code implementing new methods have comments detailing the implementation, with references to the paper where each step comes from. (yes)
- If an algorithm depends on randomness, then the method used for setting seeds is described in a way sufficient to allow replication of results. (yes)

- This paper specifies the computing infrastructure used for running experiments (hardware and software), including GPU/CPU models; amount of memory; operating system; names and versions of relevant software libraries and frameworks. (yes)
- This paper formally describes evaluation metrics used and explains the motivation for choosing these metrics. (yes)
- This paper states the number of algorithm runs used to compute each reported result. (yes)
- Analysis of experiments goes beyond single-dimensional summaries of performance (e.g., average; median) to include measures of variation, confidence, or other distributional information. (yes)
- The significance of any improvement or decrease in performance is judged using appropriate statistical tests (e.g., Wilcoxon signed-rank). (yes)
- This paper lists all final (hyper-)parameters used for each model/algorithm in the paper's experiments. (yes)
- This paper states the number and range of values tried per (hyper-) parameter during development of the paper, along with the criterion used for selecting the final parameter setting. (yes)